PCCP

Accepted Manuscript

ROYAL SOCIETY OF CHEMISTRY

www.rsc.org/pccp

Chemically Derived Defects in Zinc Oxide Nanocrystals and their Enhanced Photo-Electrocatalytic Activities

Anand Prakash and D. Bahadur*

Department of Metallurgical Engineering and Materials Science, Indian Institute of Technology Bombay
Mumbai -400 076, India

Abstract

This paper reports the influence of surface defects on the photocatalytic degradation of methylene blue (MB) for zinc oxide (ZnO) nanocrystals (NCs) synthesized in different organic solvents. A simple chemical approach has been adopted for the promotion of oxygen vacancies in pristine ZnO using solvents namely Dimethylformamide (DMF), N-Methyl-2-pyrrolidone (NMP) and Dimethylsulfoxide (DMSO). This alters the growth in NCs through the promotion of oxygen vacancies depending on the fact that the solvent with minimum viscosity supports faster nucleation and growth exhibiting maximum surface defects. DMF with minimum viscosity results in largest particle size and superior photocatalytic activity. Further, X-ray diffraction, UV-visible reflectance spectroscopy and transmission electron microscopy confirm that the DMF supports the faster growth of NCs as compared to NMP and DMSO. Electron paramagnetic resonance, Raman, X-ray photoelectron, and photoluminescence spectroscopy confirm different states of oxygen vacancies in the NCs and their dependence on the nature of the solvents. The photocatalytic activities of these NCs were investigated against degradation of MB as a model dye. The results show that the oxygen defects at the surface of NCs are more responsible for higher photocatalytic activity than the specific surface area of NCs. The electrochemical investigations of MB degradation suggest that these defects when interact with MB, influence the storage capacity and charge-discharge profiles of NCs. During degradation, MB passivates these defects, which has been accounted interns of increased charge/discharge time and storage capacity.

Keywords: ZnO, photocatalytic activities, Methylene blue (MB), surface defects (SDs), nanocrystals (NCs)

---

*Corresponding author. Fax: +91-22-25723480. Tel: +91-22-25767632.
E-mail address: dhirenb@iitb.ac.in (D. Bahadur)

1. Introduction

Wide band gap semiconductors oxide photocatalysts, such as TiO_2 and ZnO have drawn much attention because of their excellent efficiency in the degradation of organic dyes and pollutants in industrial waste [1-5]. Over the time, ZnO takes lead over TiO_2 and is believed to be a common alternative to TiO_2 due to its nontoxic nature, low cost, and high reactivity [6, 7]. The photocatalytic activity and stability of ZnO depend on many parameters such as different terminating crystal facets [8], preparation method, higher crystallinity, and increased surface area [9]. The nanostructures having large surface area with more number of active sites and high reactivity show excellent photodegradation of hazardous organic contaminants [10, 11]. These findings draw attention, which led researchers to investigate the photocatalytic activities over a range of different morphologies [12]. However, some of the ZnO nanostructures in spite of their low surface area show better degradation efficiency than the ones with higher surface area [13]. Therefore, it is necessary to understand the basic mechanism behind the photocatalytic degradation so that we could minimize the time interval for detoxification of industrial waste. Actually, the UV irradiation over these nanocrystals (NCs) results in electron-hole pairs, which eventually recombine, followed by radiative and non-radiative transitions. The suppression of e-h pair recombination either by surface orientation or by trapping at defect sites could improve their efficiency. The usual defects present in NCs are attributed to oxygen vacancies with different charged states, zinc vacancies, zinc interstitial, and could also be altered by doping with transition metal ions [14-16]. However, NCs with naturally grown oxygen defects exhibit excellent photocatalytic activity for the degradation of dyes such as methylene blue (MB) under UV light as compared to defects created by transition metal (Mn, Ni and Co) doping of ZnO [16]. These oxygen defects generally serve as photoinduced trap pockets as well as adsorption sites where the charge transfer to the adsorbed species prevents the e–h recombination. These oxygen defects are sensitive and therefore the control over these defects on the surface of the photocatalyst is essential for obtaining high photocatalytic efficiency. Wang et al [17] showed that only the optimal surface oxygen vacancy defects result in an increased photocatalytic activity.

Recently, varieties of hierarchical ZnO nanostructures with oxygen defects induced by surfactants, polymers and organic molecules have been reported [18, 19]. However, the reagents used during the synthesis are difficult to remove completely from the surface of the NCs and hence the interaction between these defects and dyes could be hindered. Such intereference slows down the photocatalytic performance of ZnO in spite of having large surface area, porosity and defects. Therefore, there is an obvious challenge to design a protocol without any surfactant or foreign molecules to control these surface oxygen defects. Over the time, the photoluminescence (PL) has become an important tool to monitor surface defects (SDs) and interfacial electron transfer in UV active NCs (ZnO, TiO_2, etc) under UV irradiation[14, 20, 21]. However, in certain cases, the defects are inherently complex and a careful deconvolution of these spectra may not be sufficient to understand photocatalytic activity thoroughly. These observations led us to think about new experimentations, which are supposed to be very sensitive towards SDs.

Our objective, in this work, is to address the photodegradation investigation of any dye (MB was taken as a model dye) through electrochemistry (charge storage and charging/discharging behavior), which has never been reported. We further wanted to study the interaction of chemically induced defects with MB and for this we synthesized ZnO NCs with different concentration of defects without any mediation (surfactants, polymers and organic molecules, etc). In this context, we chose three solvents with different viscosities/densities (Table 1), which could modify the nucleation and growth process during the hydrothermal process resulting different defect densities. The correlation of defect densities to photodegradation efficiency is an additional novelty of the present investigation. These electrochemical analyses of MB degradation are useful to understand the mechanism behind photocatalytic activity of these NCs.

2. Experimental section

2.1. Materials

Zinc acetate ($(CH_3COO)_2Zn{\cdot}2H_2O$) was purchased from Sigma-Aldrich. Dimethyl sulfoxide (DMSO) and N-methyl-2 pyrolidone (NMP) and Dimethylformamide (DMF) were purchased from Thomas Baker, India.

2.2. Synthesis of ZnO NCs

Different type of defect induced ZnO NCs were prepared by simply refluxing acetate salt in different organic solvents keeping all other reaction parameters same. The three different solvents were chosen based on the fact and assumption that minimum viscosity/density would support the faster nucleation and growth of NCs with maximum defect density. This hypothesis worked well and we observed maximum defect density and particle size when NCs were synthesized in DMF followed by NMP and DMSO (Table 1). Briefly, 920 mg of zinc acetate ($(CH_3COO)_2Zn{\cdot}2H_2O$) was dissolved in DMF (200 mL) under stirring at room temperature. The precursor was kept in an ultrasonic bath for 15 min so that acetate salt dissolved completely. Then, 4 mL of milliQ (~18 Ω-cm) was added to this precursor and was slowly heated to 145 °C for 3 h. The resultant white precipitate was washed several times with ethanol and milliQ (3 times each) to remove excess solvents and dried in vacuum oven at 50 ^{o}C for 30 min. The product was labeled as ZnO-1. The same protocol was followed except the reaction temperature, which is now 180 ^{o}C to synthesize ZnO-2 and ZnO-3 by switching

DMF with NMP and DMSO. The two processing temperatures of 145 and 180 ^{o}C were used considering the following logic: The NCs were synthesized by hydrothermal method. For this, we carefully chose the synthesis temperature generally below the boiling point (BP) of the solvents (BP of DMF ~ 154 ^{o}C whereas BP of NMP and DMSO ~ 189-202 ^{o}C) keeping all other parameters same.

2.3. Instruments and Measurements

X-ray diffraction (XRD) patterns of samples were recorded on a Philips powder diffractometer PW3040/60 with Cu Ka radiation. The thermogravimetric analysis (TGA) was performed by using SDT Q600 V8.3 Build 101 at a scan rate of 10 °C/min under inert atmosphere. The as obtained products (precipitated and dried at 50 ^{o}C) were used for TGA analysis. The phases were further confirmed by Raman measurements on Lab RAM HR 800 micro-Raman spectroscopy using the 514.5 nm line of an Argon (Ar^{+}) laser. The morphologies, structures and histogram were characterized by high-resolution transmission electron microscopy (HR-TEM, JEOL-JEM 2100F, with an accelerating voltage of 200 kV). The specific surface area, pore volume and pore size distribution of these samples were measured by ASAP 2020 Micromeritics, USA. Specific surface areas of samples were determined by the multipoint Brunauer–Emmet–Teller (BET) method. The corresponding pore size distribution and total pore volume were determined by the Brunauer Joyner-Hallenda (BJH) method applied to the desorption branch of N_2 isotherm. Before the measurements, the samples were degassed at 60 ^{o}C with a heating rate of 10 ^{o}C/min for 1 h and then the temperature was raised up to 90 ^{o}C and maintained over night.

2.4. Photocatalytic investigations

The catalytic experiments were performed at room temperature under a UV light (Philips TUV 25W/G25T8, wavelength ~ 365 nm) which was placed horizontally above the liquid surface so that catalyst could experience the maximum irradiation. Methylene blue (MB, a cationic dye) was employed as a model dye to evaluate the photocatalytic activity of the NCs having different types of oxygen defects. The procedure for the measuring the photocatalytic activity has been reported elsewhere [11]. Approximately 24.0 mg of sample was dispersed in 80 ml of MB aqueous solution (concentration ~ 10 ppm) and thoroughly mixed in an ultrasonic bath for 5 min to obtain a turbid colloidal suspension. Under continuous UV irradiation, small parts of the colloidal suspension were taken out at fixed intervals of 10 min for absorbance measurements. The strength of absorbance at 665 nm using UV–Vis spectrophotometer (Cecil, Model No. CE3021) determines the concentration of MB.

2.5. Preparation of electrodes for photo-electrocatalytic performance

The electrochemical behavior of the ZnO NCs was characterized using a three electrode electrochemical work station (CHI 660D) where glassy carbon electrode (GCE) modified with NCs works as a working electrode, a platinum wire as the counter electrode, and a saturated Ag/AgCl electrode as the reference electrode. The measurements were done in a 0.1 M Na_2SO_4 electrolyte solution in a voltage range of −0.3 to 0.8 V. The galvanostatic charge/discharge curves were measured in the voltage range of −0.3 to 0.6 V at a current density of 0.1 A/g. The preparation of working electrode involves the following steps: (1) The GCE was polished with 0.05 µm alumina powders followed by ultrasonic cleaning sequentially in isopropyl alcohol and milliQ water. Then, approximately 40 µl of suspension of NCs (2 mg ml^{-1}) was coated onto GCE and left it for air-drying. To get a response of MB, 40 µl of MB (10 ppm) was drop coated on GCE already modified with these NCs. Further MB degradation response over ZnO through electrochemistry is recorded by exposing GCE/ZnO/MB assembly under UV irradiation.

3. Results and Discussion

3.1. Structural analysis and dye degradation

The crystal structures of ZnO-1, ZnO-2 and ZnO-3 prepared in three different organic solvents were characterized by XRD. As shown in Figure1a-c, all of the diffraction peaks of the samples could easily be indexed to the crystalline wurtzite phase of ZnO (hexagonal crystal system, P63mc, JCPDS card No. 36–1451) [22]. As discussed, the role of organic solvents on the SDs induced in the NCs has been investigated, which eventually causes differences in the photocatalytic activity. Hence, it was appropriate to monitor the weight loss profiles of these NCs (Figure 2). All the ZnO NCs show different weight loss profiles with one another starting from 50 up to 800 °C. These profiles support the hypothesis that the chemical environment around these NCs strongly depends on the reaction medium. These chemical environments modify the density and type of SDs available in NCs. The single charge oxygen vacancies (V_o^+) [14, 23] are in majority in ZnO NCs and annealing helps to passivate these V_o^+ in the form of breakage of bonds and removal of oxygen. This would probably cause the weight loss above 200 °C in ZnO NCs. Further, it is established that ZnO has a tendency to lose its oxygen when annealed at higher temperatures [24]. The traces of solvents adsorbed at the NCs surface goes off below 200 °C and could be one reason behind weight loss below 200 °C. It is worth mentioning that these observations will be more prominent in the PL, EPR and XPS spectra discussed later in the report. The NCs were subjected to FEG-TEM for microstructural investigation as presented in Figure 3a-c. The microstructures of ZnO-1, ZnO-2 and ZnO-3 clearly reveal their poor monodispersity with irregular shape and size. The average diameter and distribution of NCs were estimated by considering the minimum and maximum diameter of a large number of NCs and their corresponding histograms are depicted in the insets of Figure 3a-c. It was found that the average diameter for ZnO-1 is ~ 80±5 nm and is larger than ZnO-2 (60±5) and ZnO-3 (35±5 nm). Needless to say that the chemistry of solvents plays an important role (See Table 1) in terms of difference in growth, particle diameter, and defect concentration (discussed later in the report) etc keeping reaction time (3h) constant. The analysis shows that minimum viscosity of DMF supports fastest nucleation and growth resulting maximum average diameter in case of ZnO-1 followed by ZnO-2 and ZnO-3 depending on the viscosities, which increase in the same order.

Table 1. Various physical parameters of DMF, NMP and DMSO, synthesis temperature and average particle diameter.

Solvents	Viscosity (25 ^{o}C, mPa s)	Boiling point (°C)	Density (g/ml)	Synthesis temperature (^{o}C)	Particle Size (nm)
Dimethylformamide (DMF)	0.92	154	0.944	145	80±5
N-Methyl-2 pyrrolidone (NMP)	1.7	204	1.028	180	60±5
Dimethyl sulfoxide (DMSO)	1.990	189	1.092	180	35±5

The additional information about the structures of NCs were further analysed by Raman spectroscopy- a non-destructive technique used for crystallographic identification in nanomaterials. Figure 4 shows the room temperature Raman spectra of the ZnO NCs in the range of 200-1500 cm^{-1}. A sharp peak in the range of 437.5-438.5 cm^{-1} is noted for all and could be assigned to the nonpolar optical phonon E_2 (high) mode in ZnO [22]. The existence of the E_2 (high) mode indicates the hexagonal wurtzite structure, which is in agreement with the XRD. However, the E_2 mode involves only the oxygen atoms associated with the lattice and the strongest peak seen in ZnO-1 anticipates maximum SDs in ZnO-1 [25]. The availability of maximum defects density in ZnO-1 as compared to ZnO-2 and ZnO-3 is more evident in EPR, PL and XPS spectra discussed later.

N_2 adsorption/desorption isotherms measurements are conducted to investigate the Brunauer–Emmett–Teller (BET) specific surface area and porosity of as-prepared ZnO NCs

(Figure 5). The specific surface area (Figure 5d) is maximum in case of ZnO-3 (31.78 m^2g^{-1}), followed by ZnO-2 (18.37 m^2g^{-1}) and is minimum for ZnO-1 (13.21 m^2 g^{-1}). The other textural properties such as total pore volume of samples are listed in table 2. The isotherms for these NCs are close to Type IV with an evident hysteresis loop in the range of 0.80-0.99 relative pressure (P/Po), indicating the mesoporous structures (Figure 5a-c) formed in NCs [26, 27]. The corresponding pore size distributions calculated by the Barrett–Joyner–Halenda (BJH) method, are given in the insets of Figure 5. The distribution of pores in ZnO-1 and ZnO-2 lies in between 200 -1200 nm whereas ZnO-3 shows a narrow pore size distribution spread in between 50-400 nm.

Table 2. Textural analysis of ZnO NCs

Samples	BET (m^2/g)	Single point adsorption total pore volume of pores cm^3/g
ZnO-1	13.21	0.17
ZnO-2	18.37	0.24
ZnO-3	31.78	0.19

The UV-Vis absorption spectra in Figure 6 show that for ZnO-1 and ZnO-2, the absorption edges centre in between ~375-372 nm and correspond to electronic transitions between the valence and conduction bands[28] whereas ZnO-3 exhibits a blue-shift of ~ 5 nm with an absorption edge at 366 nm (Inset of Figure 6). Further, ZnO-1 shows prominent absorbance even in visible light region followed by ZnO-2 and is minimized for ZnO-3. We propose that the reaction medium induces the SDs in ZnO samples and their population follows the same order as seen in their absorbance spectra. These SDs eventually hinder the fundamental process of electron–hole pair recombination during UV irradiation [29] and might be one of the reasons for superior photocatalytic activity exhibited by ZnO-1 discussed in the next section.

The photocatalytic degradation of MB in the presence of the defect induced mesoporous ZnO NCs as catalysts under UV irradiation have been investigated. The UV-Vis response of MB in presence of ZnO catalysts under UV for different time intervals are shown in Figure 7a-c. As exposure time increases, the successive reduction in characteristic absorption band intensities of MB at 665 nm indicates degradation of MB by ZnO (Figure 7a-c). Figure 7d represents the relative degradation of MB versus time where Co and C are the initial and the remaining concentration of MB at time t respectively. The ZnO-1 degrades MB faster than ZnO-2 (60 min) and ZnO-3 (70 min) and achieves complete degradation of MB in just 30 min. The specific surface area and porosity of nanomaterials are important parameters in determining the degradation efficiency of dyes. The surface area provides the active sites whereas pores help to trap these dyes and their synergic effects enhance the catalytic efficiency of nanomaterials. These concepts anticipate that either ZnO-3 with highest surface area or ZnO-2 with maximum pore volume should show superior catalytic activity. However, the experimental data shows that ZnO-1 shows the best catalytic activity in spite of lowest surface area and pore volume. Recently, it has been reported by many researchers that SDs can not be neglected and is certainly an important parameter in determining the catalytic activity [11, 30]. Both XPS and PL responses are sensitive to these SDs. A close observation of Z2p and O1s bands of ZnO samples in XPS spectra results a link to corresponding PL signals. These analyses help to correlate the degradation efficiency to the SDs. The XPS spectra of ZnO NCs are presented in Figure S1-A where survey spectra between 200 and 1200 eV bring out the characteristic bands of $Zn2p_{1/2}$, $Zn2p_{3/2}$, and O1s only. This further rules out the existence to any other phases or contamination during the growth of these NCs. Figure S1-B shows high-resolution XPS peaks of Zn2p core level of ZnO–1, ZnO-2 and ZnO-3 respectively. The ZnO-1 shows doublet spectral lines at 1022 eV ($Zn2p_{3/2}$) and 1045 eV ($Zn2p_{1/2}$) with a spin–orbit splitting (ΔE) of 23.0 eV. In contrast, the peak positions of doublet spectral lines (Zn2P) of

ZnO–2 and ZnO-3 are at slightly lower binding energies with a corresponding higher spin–orbit splitting (ΔE) of 23.4 and 23.6 eV.

The O1s spectrum of the ZnO could be ideally thought of being comprised of two factors depending on the concentration of oxygen vacancies. Therefore, the typical O1s peaks of samples are deconvoluted into two Gaussian peaks: (1) the first one centers at higher binding energies and are in between 533.5-531.8 eV. These energy peaks are assigned to loosely bound oxygen (from sources such as adsorbed H_2O or O_2) atoms on the surface of the NCs and are attributed to the oxygen-deficient regions in ZnO [31]. (2) The second one resides at lower binding energy (~ 530.9-531.3 eV) and is attributed to the O^{2-} ion (Zn–O bonding) in the wurtzite structure of hexagonal ZnO [32]. The changes in the relative intensity of these components could be connected to the variations in the concentration of the oxygen vacancies. The ratio of intensities of the higher and lower binding energy peak (P_H/P_L) is highest in ZnO-1 being weaker in ZnO-2 and is minimum in ZnO-3. Needless to say that the area under the O1s curve which could determine the density of SDs is maximum in ZnO-1 followed by ZnO-2 and is minimum in ZnO-3. These results indicate that even if the size of ZnO-3 is much smaller than ZnO-1, the later possess maximum SDs. The concept of solvent mediated SDs is further confirmed by PL spectra, which also helps to understand the charge transfer mechanism under UV irradiation. The PL spectra of all the samples are shown in Figure 9. Generally, the PL spectrum of ZnO results a sharp near-band-edge (NBE) transition (382 nm) accompanied with a broad defect related green-orange band (480–750 nm) [13, 29]. Similar to XPS, the differences in the shape and position of the visible emission peak may indicate various types of SDs. A comparison of the PL spectra of ZnO samples are illustrated in Figure 9. As compared to UV emission peak in each NCs, the defect band is strongest in ZnO-1, being weaker in ZnO-2 and is minimum in ZnO-3. Different hypotheses have been proposed in the literature behind the origin of these emissions. Some of them are associated with various kind of SDs as discussed in the introduction [33] and the band normally appears when electron–hole recombines at a deep level, caused by these SDs . To get a deeper insight about the role of reaction medium, we have also deconvoluted the defect band spectrum of each sample into three separate bands: (I) at ~480–550 nm (blue-green), (II) at ~550–610 nm (yellow) and (III) at ~ 610–750 nm (orange) respectively. It is now experimentally established that the band at lower wavelength (blue-green) originates from the singly charged oxygen vacancy (V_{os}^{+}), the middle one (yellow) is commonly attributed to the doubly charged oxygen vacancies (V_{os}^{++}) [34]. In contrast, oxygen interstitials and defect complexes possibly involving zinc vacancies have been proposed for orange-red emission at higher wavelength [35]. The intensity of blue emission is stronger than orange emission in ZnO-1. It starts shrinking, and becomes comparable to orange emission in ZnO-2, and finally suppressed in ZnO-3. The ratio intensities of deconvoluted bands are given in table 3. These results indicate that near band edge (NBE) emission and intensity of visible emission is also dependent on the reaction medium in addition to the size, morphology, method of preparation, and surface treatment of the ZnO nanostructures.

Table 3. Summary of the PL spectra of different ZnO NCs

Samples	INBE/I	I/III	II/III
ZnO-1	0.15	1.98	2.59
ZnO-2	0.13	1.13	1.64
ZnO-3	2.9	0.49	1.01

Thus, PL emission is a measure of the recombination rate of excited electrons and holes and a lower NBE along with higher visible emission having larger concentration of the surface oxygen vacancies is a guarantee of minimization of recombination rates. This eventually results excellent photocatalytic oxidation activity shown by ZnO-1 over ZnO-2 and ZnO-3 as shown in Figure 7. The present results suggest that in spite of minimum surface area and pore volume, ZnO-1 shows the best photocatalytic activity towards MB and is attributed to the density of oxygen vacancies.

3.2. Photo-electrochemical studies of MB under UV irradiation

The electrochemical response is extremely sensitive towards surface modification, size and doping of nanomaterials [21, 36, 37]. Although, the technique has already been demonstrated for selective label-free detection of cancer cells [38], heavy metal cations [27] and supercapacitors [39] etc yet its responses over dyes before and after UV irradiation in the presence of ZnO have rarely been investigated. These investigations could help us to understand that how is MB interacting with SDs during its degradation under UV. We investigate these interactions in terms of charge capacity of ZnO in presence of MB and under UV. We performed the electrochemical studies on all ZnO samples in 0.1 M Na_2SO_4 and extended our studies on MB deposited over ZnO-1 by recording its responses before and after UV irradiation due to superior degradation efficiency of ZnO-1 over the other samples. Figure 10a shows the CV responses of all NCs, which are slightly rectangular in shape at a constant voltage sweep rate of 50 mV/s. This indicates good charge propagation at the electrode/electrolyte interfaces, possessing an electrical double layer (EDL) and a low contact resistance at the interface [40]. However, the area under the CV curve is an important parameter, which determines the materials capability to hold charges in the form of EDLs and eventually electrical energy. The area under the curve possess by ZnO-1 is minimum followed by ZnO-2 and is maximum in ZnO-3. Thus, the highest current response in the cyclic voltammograms of ZnO-3 indicates the best capacitive performance. We have already discussed that ZnO-1 has the maximum defects followed by ZnO-2 and is minimum in ZnO-3. Thus, ZnO-1 with maximum SDs shows minimum charge storage capacity (Figure 10a).

To obtain more information about the SDs dependence on the charge storage capacity, galvanostatic charge/discharge measurements were carried out as shown Figure 10b. Likewise, the charge/discharge time taken by ZnO-1 is minimum followed by ZnO-2 and is maximized in ZnO-3. The symmetry between charge/discharge curve, which accounts for a reversible Faradic reaction between Na^+ and ZnO, is completely lost in ZnO-3. In addition, the longest discharging time in ZnO-3 represents its minimum charge transfer resistance towards electrolytes and highest capacitance over others as shown by the CV curves depicted in Figure 10a. These results further strengthen our belief that electrochemical behaviour of nanomaterials could be easily linked with the SDs and higher SDs is responsible for inferior charge capacity. Since, ZnO-1 shows superior degradation efficiency towards MB under UV, we recorded the CV responses of MB in presence of ZnO-1 and compared it with the responses when MB is completely degraded under UV. Both CV and charge/discharge time of ZnO-1 in the presence of MB is higher than pristine ZnO-1 (Figure 10-c, d). This reflects that MB interacts with the SDs and somehow passivates it via interfacial charge transfer. This leads to increase of charge storage capacity and charge/discharge time in ZnO-1. Further, to understand the degradation behavior of MB, we have also recorded the CV as well as charge-discharge behavior of MB in presence of ZnO-1 after UV irradiation (Figure 10-b, c). Both capacitive behavior as well as charge-discharge time of ZnO-1 increased after degradation of MB. This shows that passivation of defects is more effective when MB is completely degraded by ZnO-1. Thus, the excellent degradation of MB by ZnO-1 is due to trapping of more photogenerated electron at the defect sites. These results are further accountable in terms of enhancement in charge storage capacity and charge-discharge time.

4. Conclusions

We have synthesized mesoporous ZnO NCs in which SDs are chemically induced through the different reaction medium. Under same reaction parameters, DMF with minimum viscosity supports fastest growth of NCs (ZnO-1) followed by NMP (ZnO-2) and DMSO (ZnO-3) as viscosity/density increase. The results of photocatalytic experiments suggest that the efficiency depends on SDs and ZnO-1 with maximum SDs achieves fastest decolourization of MB. We find that green and orange emissions depend on the reaction medium and faster photocatalytic activity is achieved with strong green emission. The electrochemical studies suggest that ZnO-1 shows poorer charge storage capacity and charge/discharge time due to more SDs as compared to other two samples (ZnO-2 and ZnO-3). The degradation of MB under UV results faster passivation of these SDs, which is reflected in terms of larger charge storage capacity and charge/discharge time in electrochemical investigation.

Electronic Supplementary Information

X-ray photoelectron (XPS) survey spectra and Zn2p doublet spectral lines of ZnO-1, ZnO-2 and ZnO-3. Electron paramagnetic resonance (EPR) spectra and hydrodynamic diameter (nm) of ZnO-1, ZnO-2 and ZnO-3 NCs

Author Information

***Corresponding Author**
Fax: +91-22-25723480. Tel: +91-22-25767632.
E-mail address: dhirenb@iitb.ac.in (D. Bahadur)

Acknowledgments

Financial supports from Nanomission, Department of Science and Technology (DST), Government of India is gratefully acknowledged. The authors are thankful to the Centre for Research in Nanotechnology & Science (CRNTS) for FEG-TEM and Raman facilities. The authors also thanks to Dr. D.S. Sutar for XPS measurements at Central Surface Analytical Facility, IIT Bombay

References and notes

1. U. I. Gaya and A. H. Abdullah, *J. Photochem. Photobiol., C*, 2008, 9, 1-12.
2. M. R. Hoffmann, S. T. Martin, W. Choi and D. W. Bahnemann, *Chem. Rev.*, 1995, 95, 69-96.
3. R. Daghrir, P. Drogui and D. Robert, *Ind. Eng. Chem. Res.*, 2013, 52, 3581-3599.
4. S. Singh, K. Barick and D. Bahadur, *Nanotechnology and Nanomaterials*, 2013, 3, 1-20.
5. S. Humaira, K. C. Kemp, C. Vimlesh and S. K. Kwang, *Nanotechnology*, 2012, 23, 355705.
6. C. Lizama, J. Freer, J. Baeza and H. D. Mansilla, *Catal. Today*, 2002, 76, 235-246.
7. N. Daneshvar, D. Salari and A. R. Khataee, *J. Photochem. Photobiol., A*, 2004, 162, 317-322.
8. N. Kislov, J. Lahiri, H. Verma, D. Y. Goswami, E. Stefanakos and M. Batzill, *Langmuir*, 2009, 25, 3310-3315.
9. M. Y. Guo, A. M. C. Ng, F. Liu, A. B. Djurišić, W. K. Chan, H. Su and K. S. Wong, *J. Phys. Chem. C*, 2011, 115, 11095-11101.
10. H. B. Lu, H. Li, L. Liao, Y. Tian, M. Shuai, J. C. Li, M. F. Hu, Q. Fu and B. P. Zhu, *Nanotechnology*, 2008, 19, 045605.
11. S. Singh, K. C. Barick and D. Bahadur, *CrystEngComm*, 2013, 15, 4631-4639.
12. J. Gupta, K. C. Barick and D. Bahadur, *J. Alloys Compd.*, 2011, 509, 6725-6730.
13. J. H. Zeng, B. B. Jin and Y. F. Wang, *Chem. Phys. Lett.*, 2009, 472, 90-95.
14. B. Panigrahy, M. Aslam, D. S. Misra, M. Ghosh and D. Bahadur, *Adv. Funct. Mater.*, 2010, 20, 1161-1165.
15. A. Janotti and C. G. Van de Walle, *Physical Review B*, 2007, 76.

16. K. C. Barick, S. Singh, M. Aslam and D. Bahadur, *Microporous Mesoporous Mater.*, 2010, 134, 195-202.

17. H. Wang and C. Xie, *Physica E: Low-dimensional Systems and Nanostructures*, 2008, 40, 2724-2729.

18. F. Liu, Y. H. Leung, A. B. Djurišić, A. M. C. Ng and W. K. Chan, *J. Phys. Chem. C*, 2013, 117, 12218-12228.

19. X. Pan, M.-Q. Yang and Y.-J. Xu, *Phys. Chem. Chem. Phys.*, 2014, 16, 5589-5599.

20. G. Williams and P. V. Kamat, *Langmuir*, 2009, 25, 13869-13873.

21. A. Prakash, N. S. Singh and D. Bahadur, *Mater. Chem. Phys.*, 2014, 144, 529-537.

22. A. Prakash, S. K. Misra and D. Bahadur, *Nanotechnology*, 2013, 24, 095705.

23. X. Xu, C. Xu, J. Dai, J. Hu, F. Li and S. Zhang, *J. Phys. Chem. C*, 2012, 116, 8813-8818.

24. L. C. Ann, S. Mahmud and S. K. M. Bakhori, *Appl. Surf. Sci.*, 2013, 265, 137-144.

25. J. Sang-Hun, K. Jae-keun and L. Byung-Teak, *J. Phys. D: Appl. Phys.*, 2003, 36, 2017.

26. K. S. W. Sing, D. H. Everett, R. A. W. Haul, L. Moscou, R. A. Pierotti, J. Rouquerol and T. Siemieniewska, *Pure Appl. Chem.,* 1985, 57, 603-619.

27. A. Prakash, S. Chandra and D. Bahadur, *Carbon*, 2012, 50, 4209-4219.

28. D. Segets, J. Gradl, R. K. Taylor, V. Vassilev and W. Peukert, *ACS Nano*, 2009, 3, 1703-1710.

29. Y. Lv, W. Yao, X. Ma, C. Pan, R. Zong and Y. Zhu, *Catal. Sci. Technol.*, 2013, 3, 3136.

30. Y. Sun, G. M. Fuge, N. A. Fox, D. J. Riley and M. N. R. Ashfold, *Adv. Mater.*, 2005, 17, 2477-2481.

31. S. A. Ansari, M. M. Khan, S. Kalathil, A. Nisar, J. Lee and M. H. Cho, *Nanoscale*, 2013, 5, 9238.

32. C. C. Li, Z. F. Du, L. M. Li, H. C. Yu, Q. Wan and T. H. Wang, *Appl. Phys. Lett.*, 2007, 91, -.

33. A. B. Djurišić, Y. H. Leung, K. H. Tam, Y. F. Hsu, L. Ding, W. K. Ge, Y. C. Zhong, K. S. Wong, W. K. Chan, H. L. Tam, K. W. Cheah, W. M. Kwok and D. L. Phillips, *Nanotechnology*, 2007, 18, 095702.

34. A. van Dijken, J. Makkinje and A. Meijerink, *J. Lumin.*, 2001, 92, 323-328.

35. Y. Zuo, S. Ge, Z. Chen, L. Zhang, X. Zhou and S. Yan, *J. Alloys Compd.*, 2009, 470, 47-50.

36. A. P. Bhirud, S. D. Sathaye, R. P. Waichal, L. K. Nikam and B. B. Kale, *Green Chem.*, 2012, 14, 2790-2798.

37. S. Wu, Q. He, C. Tan, Y. Wang and H. Zhang, *Small*, 2013, 9, 1160-1172.

38. S. Chandra, N. Barola and D. Bahadur, *Chem. Commun.*, 2011, 47, 11258-11260.

39. A. Prakash and D. Bahadur, *ACS Appl. Mater. Interfaces*, 2014, 6, 1394-1405.

40. M. D. Stoller, S. Park, Y. Zhu, J. An and R. S. Ruoff, *Nano Lett*, 2008, 8, 3498-3502.

FIGURE CAPTIONS

Figure 1. XRD patterns of (a) ZnO-1, (b) ZnO-2, and (c) ZnO-3.

Figure 2. TG curves of as-prepared ZnO NCs synthesized in different organic solvents.

Figure 3. TEM micrographs of as prepared (a) ZnO-1, (b) ZnO-2, and (c) ZnO-3. Insets show histograms of particle size distribution for the same.

Figure 4. Raman spectra of (a) ZnO-1, (b) ZnO-2 and (c) ZnO-3.

Figure 5. Nitrogen adsorption/desorption isotherms of (a) ZnO-1, (b) ZnO-2, (c) ZnO-3. The insets show the porosity distribution. (d) BET plots of ZnO-1, ZnO-2 and ZnO-3. The P_o and P are the equilibrium and the saturation pressure.

Figure 6. UV–Vis absorption spectra of (a) ZnO-1, (b) ZnO-2 and (c) ZnO-3. The inset shows the enlarged view of absorption spectra in the range of 325-410 nm and demonstrates blue shift in ZnO-3.

Figure 7. (a-c) UV–Vis spectra of MB in presence of ZnO-1, ZnO-2 and ZnO-3 before and after different time intervals of UV irradiation.(d) Comparison of degradation performance of methylene blue (MB) under UV irradiation in the presence of ZnO-1, ZnO-2 and ZnO-3.

Figure 8. (a-c) The O1s spectra of ZnO-1, ZnO-2 and ZnO-3. The area under the curve in each sample determines the density of SDs whereas the position and intensity deconvoluted peaks decides the nature of SDs or loosely bound oxygen contents.

Figure 9. (a) The RT PL spectra of ZnO-1, ZnO-2 and ZnO-3 respectively. (b-d) The broad visible emissions of ZnO NCs have been deconvoluted into three prominent peak centered in between following wavelengths ranges: I ≈ 475-515(blue emission), II ≈ 525-575 (green emission) and III ≈ 625-675 (orange-red emission).

Figure 10. (a, b) CVs and charge-discharge profiles of ZnO-1, ZnO-2 and ZnO-3 modified GCE electrodes in 0.1 M Na_2SO_4. (c, d) The CVs and charge-discharge responses of ZnO-1 in presence of MB before and after degradation under UV exposure.

LIST OF FIGURES

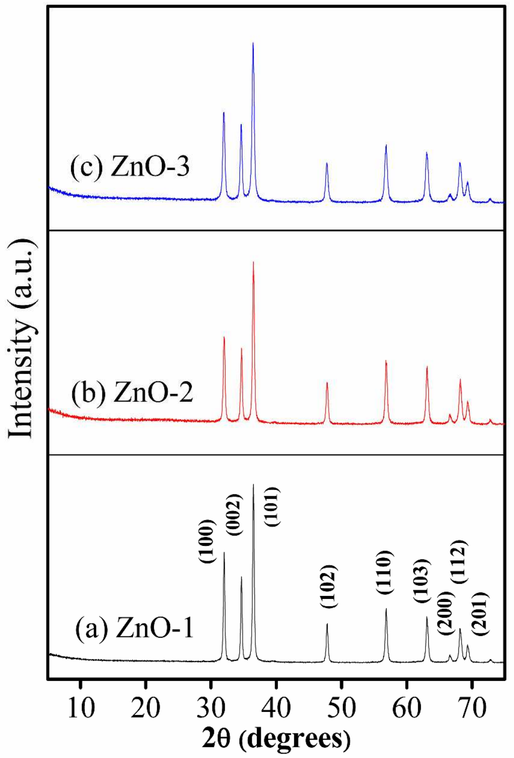

Figure 1. XRD patterns of (a) ZnO-1, (b) ZnO-2, and (c) ZnO-3.

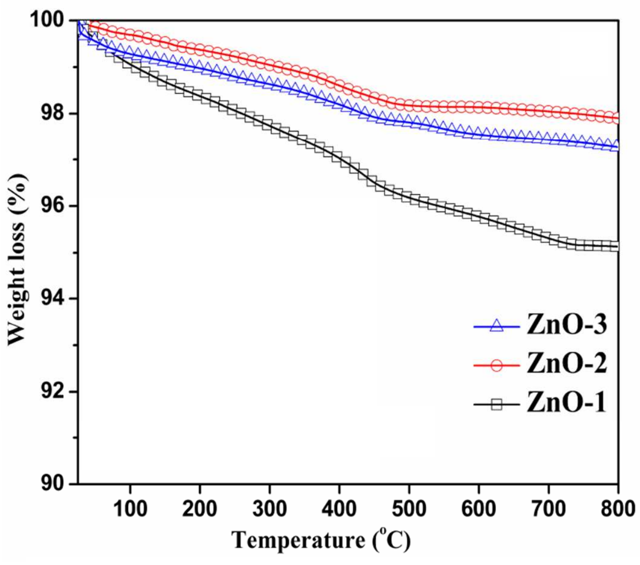

Figure 2. TG curves of as-prepared ZnO NCs synthesized in different organic solvents.

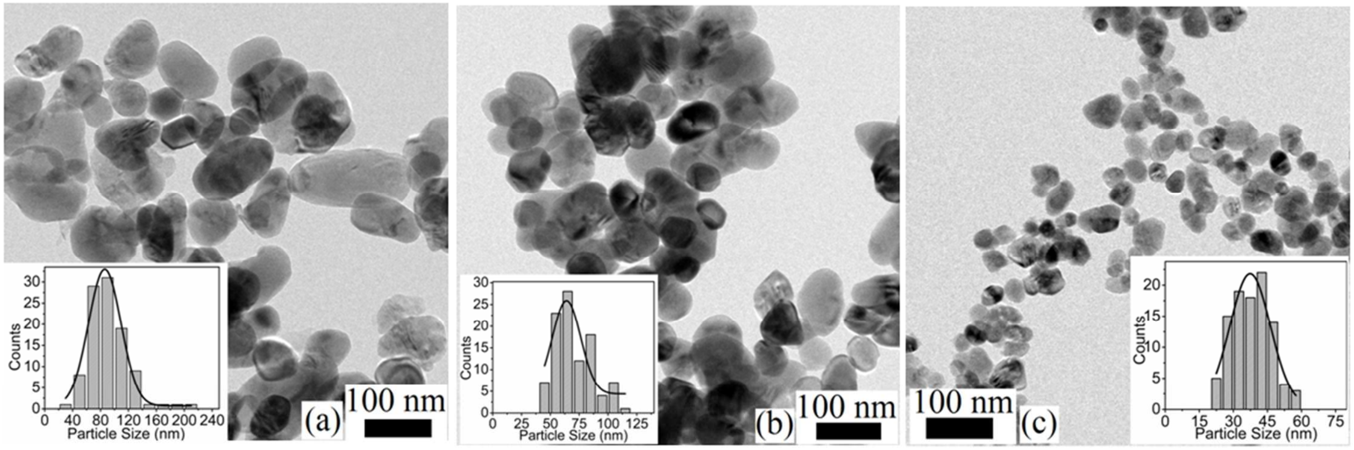

Figure 3. TEM micrographs of as prepared (a) ZnO-1, (b) ZnO-2, and (c) ZnO-3. Insets show histograms of particle size distribution for the same.

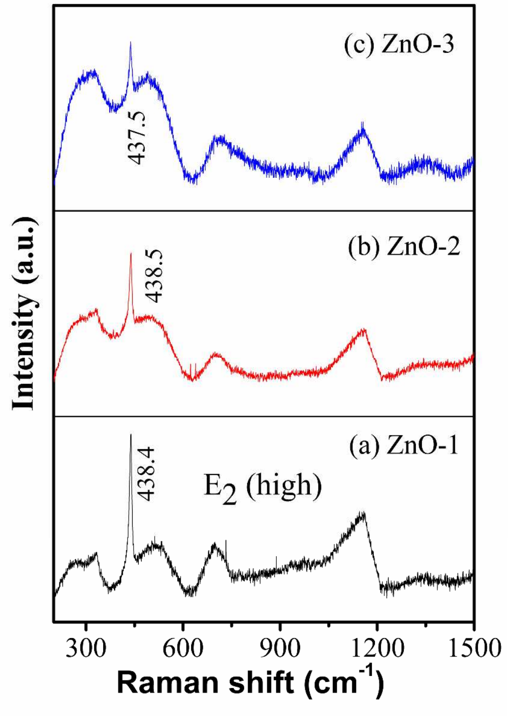

Figure 4. Raman spectra of (a) ZnO-1, (b) ZnO-2 and (c) ZnO-3.

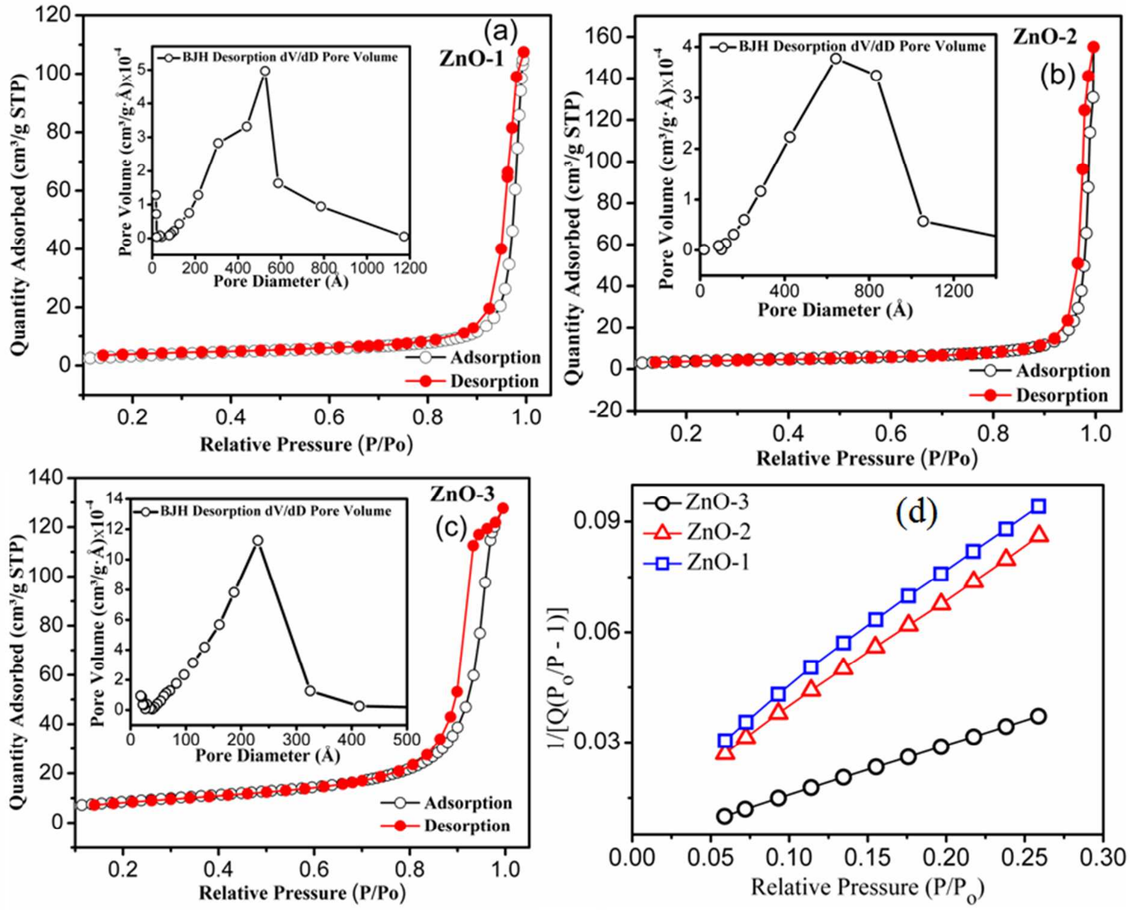

Figure 5. Nitrogen adsorption/desorption isotherms of (a) ZnO-1, (b) ZnO-2, (c) ZnO-3. The insets show the porosity distribution. (d) BET plots of ZnO-1, ZnO-2 and ZnO-3. The P_o and P are the equilibrium and the saturation pressure.

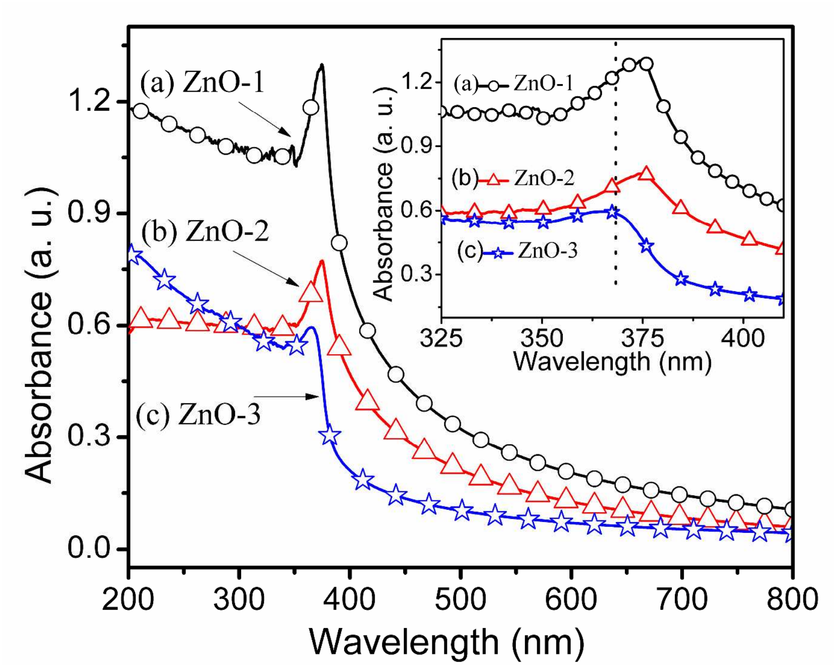

Figure 6. UV–Vis absorption spectra of (a) ZnO-1, (b) ZnO-2 and (c) ZnO-3. The inset shows the enlarged view of absorption spectra in the range of 325-410 nm and demonstrates blue shift in ZnO-3.

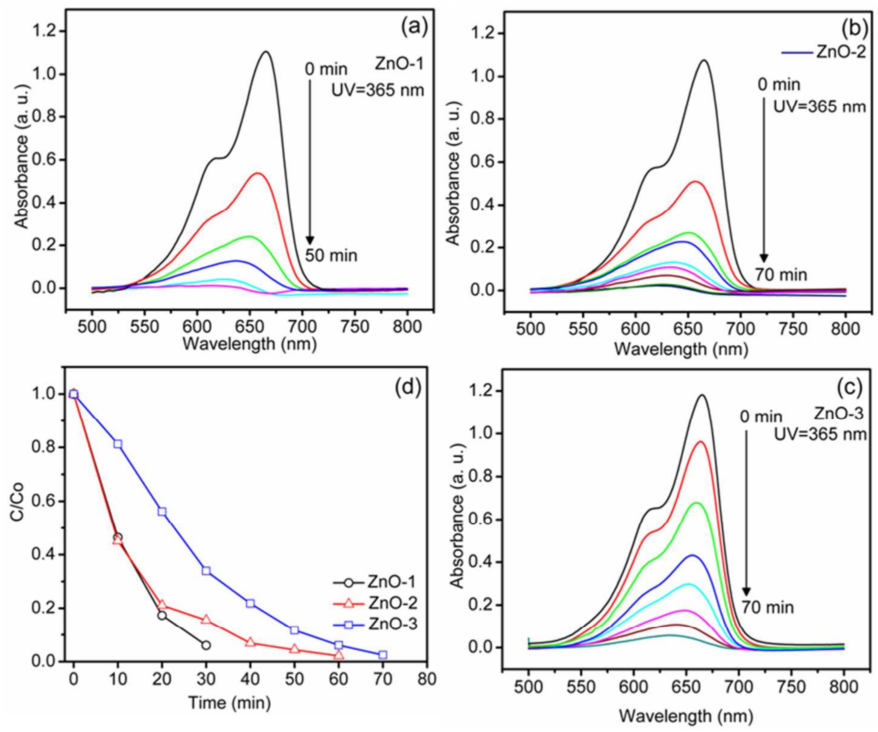

Figure 7. (a-c) UV–Vis spectra of MB in presence of ZnO-1, ZnO-2 and ZnO-3 before and after different time intervals of UV irradiation.(d) Comparison of degradation performance of methylene blue (MB) under UV irradiation in the presence of ZnO-1, ZnO-2 and ZnO-3.

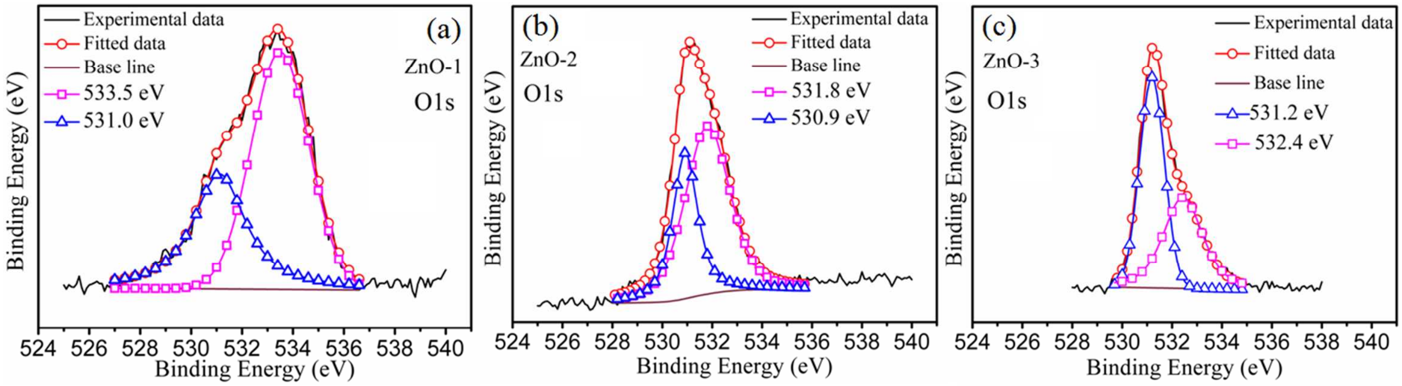

Figure 8. (a-c) The O1s spectra of ZnO-1, ZnO-2 and ZnO-3. The area under the curve in each sample determines the density of SDs whereas the position and intensity deconvoluted peaks decides the nature of SDs or loosely bound oxygen contents.

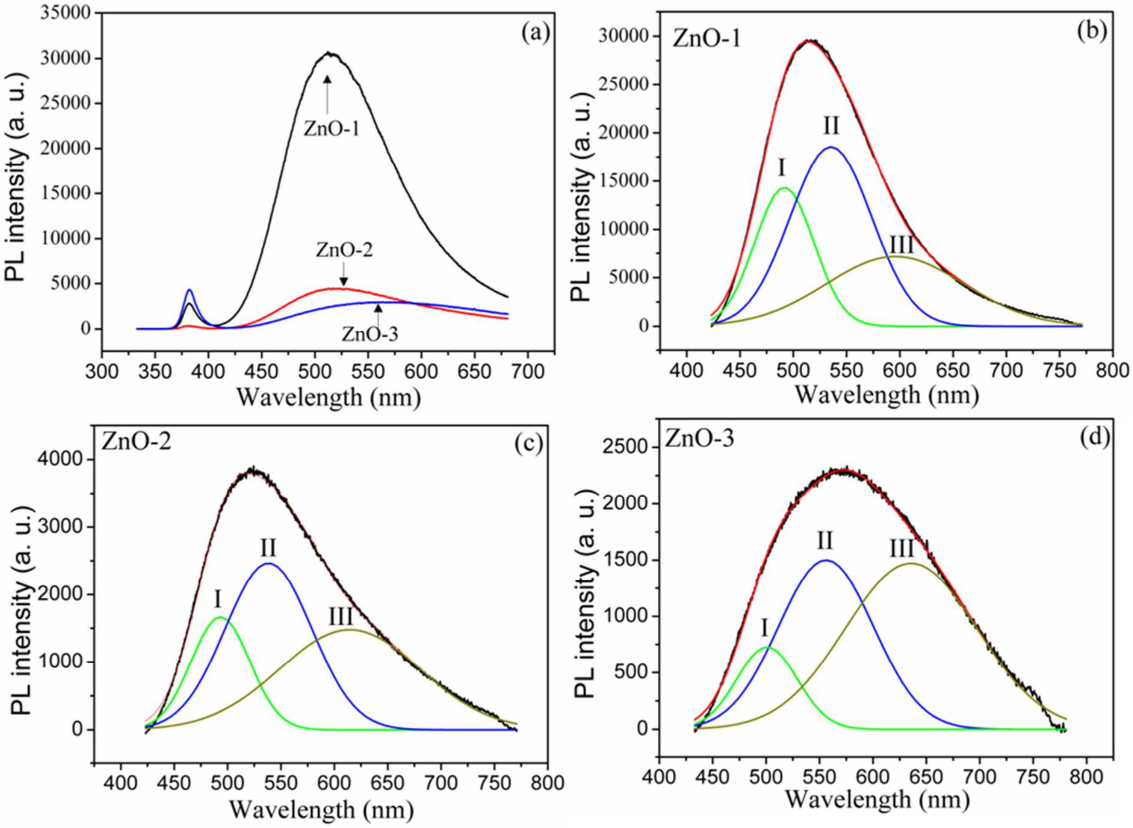

Figure 9. (a) The RT PL spectra of ZnO-1, ZnO-2 and ZnO-3 respectively. (b-d) The broad visible emissions of ZnO NCs have been deconvoluted into three prominent peak centered in between following wavelengths ranges: I ≈ 475-515(blue emission), II ≈ 525-575 (green emission) and III ≈ 625-675 (orange-red emission).

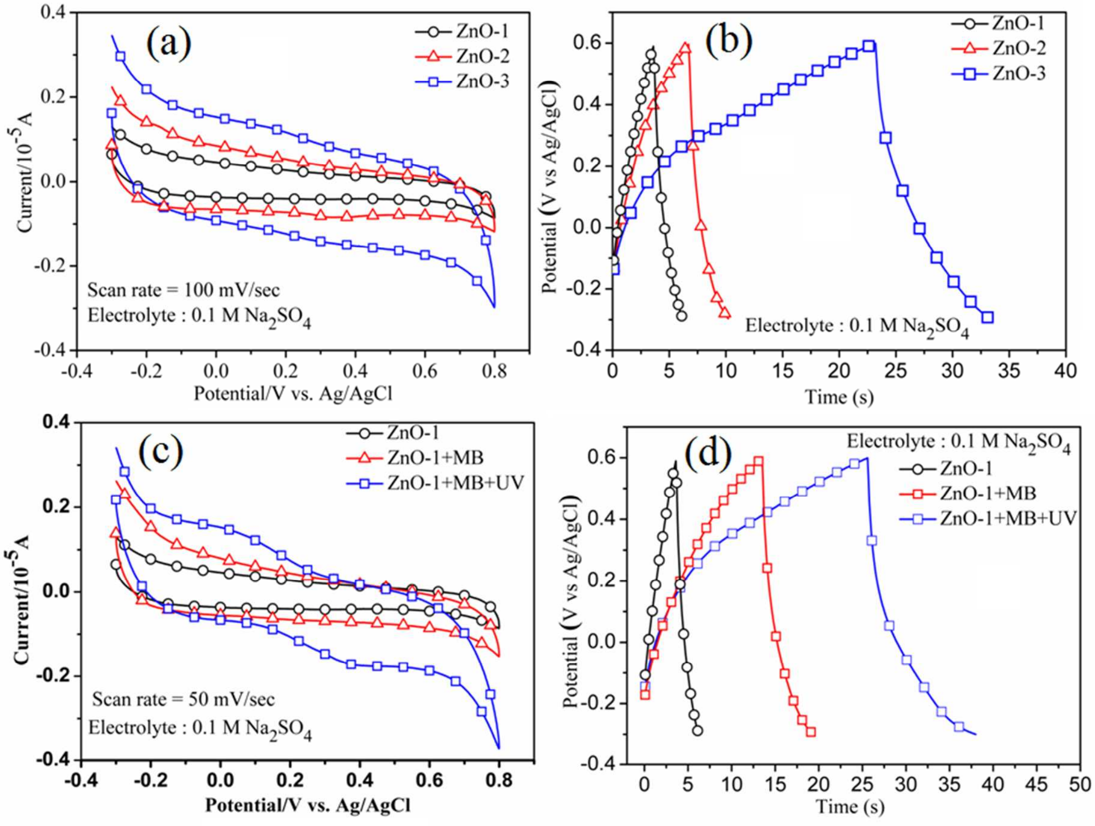

Figure 10. (a, b) CVs and charge-discharge profiles of ZnO-1, ZnO-2 and ZnO-3 modified GCE electrodes in 0.1 M Na_2SO_4. (c, d) The CVs and charge-discharge responses of ZnO-1 in presence of MB before and after degradation under UV exposure.